

Multi-Modal Monitoring of Slip Along Frictional Discontinuities

Ahmadreza Hedayat · Laura J. Pyrak-Nolte · Antonio Bobet

Received: 31 March 2014 / Accepted: 4 April 2014
© Springer-Verlag Wien 2014

Abstract Seismic wave transmission and digital image correlation (DIC) are employed to study slip processes along frictional discontinuities. A series of biaxial compression experiments are performed on gypsum specimens with non-homogeneous contact surfaces. The specimens are composed of two blocks with perfectly mated contact surfaces with a smooth surface with low frictional strength on the upper half and a rough surface with high frictional strength on the lower half. Compressional, P, and shear, S, wave pulses were transmitted through the discontinuity while digital images of the specimen surface were acquired during the test. A distinct peak in the amplitude of transmitted wave occurs prior to the peak shear strength and is considered a “precursor” to the failure. Precursors indicate that slip initiates from the smooth surface and extends to the rough surface as the shear load is increased. From the DIC data, slip is identified as a jump in the displacement field along the fracture that initiates from the smooth surface and propagates to the rough surface. Precursors are associated with an increase in the rate of slip across the

discontinuity and are a measure of the reduction in the fracture shear stiffness.

Keywords Seismic wave transmission · Digital image correlation · Frictional discontinuity · Shear stiffness

1 Introduction

The strength and deformation behavior of rocks are significantly influenced by the presence of discontinuities and fractures in the rock mass. Shearing is a common mode of failure in rock engineering and shear strength along discontinuities plays a major role in the stability of underground structures and rock slopes. The frictional behavior of rock joints has been of interest to many scientists and engineers (e.g. Ladanyi and Archambault 1969; Jaeger 1971; Barton 1976; Barton and Choubey 1977; Byerlee 1978; Dieterich 1979; Jaeger et al. 2007).

The shear strength of rock joints depends on the level of effective normal stress applied on the plane of sliding, the rock type, the roughness of the joint surface, the size of the joint (scale effect), and the environmental conditions (e.g., presence of water and pore pressure) (Byerlee 1978; Kulatilake et al. 1995; Brady and Brown 2004; Jaeger et al. 2007). Extensive research has been performed to evaluate slip along fully persistent homogeneous discontinuities with uniform frictional resistance. Although commonly assumed to be uniform, slip along a discontinuity is non-uniform and may not occur simultaneously along the entire surface of the discontinuity (De Bremaecker 1987; Price 1988; Sibson 1989; Mutlu and Bobet 2006). Slip may initiate from a region of low frictional resistance and spread asymmetrically to regions with higher resistance resulting in non-uniform normal and shear stress

A. Hedayat (✉)
Department of Engineering, Indiana University-Purdue
University, Fort Wayne, IN 46805, USA
e-mail: hedayata@ipfw.edu

L. J. Pyrak-Nolte · A. Bobet
School of Civil Engineering, Purdue University, W. Lafayette,
IN 47907, USA

L. J. Pyrak-Nolte
Department of Physics, Purdue University, W. Lafayette,
IN 47907, USA

L. J. Pyrak-Nolte
Department of Earth, Atmospheric and Planetary Sciences,
Purdue University, W. Lafayette, IN 47907, USA

distributions along the discontinuity (Comninou and Dundurs 1983; Gorbatiikh et al. 2001; Malanchuk 2011). In faults and at large scales, slip distributions are often asymmetric. Non-uniform slip distributions may be caused by variations in frictional strength along a joint or fault, non-uniform stress fields, inelastic deformations near fault terminations and variations in the elastic modulus of the host rock (Bürgmann et al. 1994). Also, careful observation of some moderate earthquakes reveals that the size of the nucleation region responsible for the earthquake is of orders of magnitude smaller than the overall rupture surface (Johnston et al. 1987; Lockner 1993). Therefore, assuming a “uniform” frictional resistance along a discontinuity may not be appropriate and may result in an unsafe design (Mutlu and Bobet 2005).

Active seismic monitoring, in particular compressional and shear wave propagation, has been used as a successful technique to observe local changes in the physical properties of a fracture (Hudson 1981; Yoshika and Scholz 1989; Pyrak-Nolte et al. 1990; Chen et al. 1993; Hildyard et al. 2005; Nagata et al. 2008). In this work, the seismic monitoring method uses an array of electronically activated transducers to transmit ultrasonic waves through the rock to an array of receivers. The seismic wave monitoring technique provides a continuous and non-destructive way to probe the internal structure of the rock. Seismically, a fracture behaves as a low-pass filter that attenuates the high-frequency components of the signal (King et al. 1986; Pyrak-Nolte et al. 1990).

In the field of experimental fracture mechanics, a relatively new technique called Digital Image Correlation (DIC) has gained popularity in measuring surface deformations. DIC directly computes the full-field surface deformations by comparing the digital images taken before and after deformation through digital image processing and numerical computing (Chu et al. 1985; Liu and Iskander 2004; Rechenmacher and Finno 2004; Withers 2008; Orteu 2009; Pan et al. 2009; Sutton et al. 2009; Lin and Labuz 2013). DIC has a great potential for evaluating slip by computing relative vertical displacements along the discontinuity. In this paper, seismic wave transmission measurements are coupled with the DIC technique to monitor slip initiation and propagation processes along discontinuities because active seismic monitoring enables observations of the internal changes along a frictional surface.

2 Digital Image Correlation

The DIC technique is a modern particle tracking method by which the deformations of small regions of an image are measured by comparing images at different instances of the

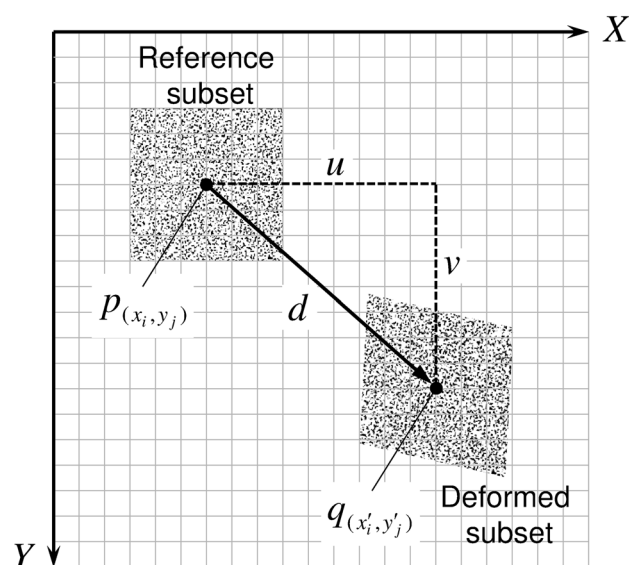


Fig. 1 Schematic illustration of the reference and deformed subsets

deformation process. The main assumption in DIC is that the displacements of the image correspond to the displacements of the object surface. By comparing the digital images of the specimen, before and after deformation, DIC provides the full-field displacement. Typically, implementation of the DIC method requires three steps: specimen surface preparation, image acquisition, and image correlation.

In two-dimensional DIC, only one charge-coupled device (CCD) camera is needed to acquire the digital images during the experiment. Depending on the intensity of light reflected from a point on the object surface, a cell in the array of pixels embedded in the CCD camera stores the grey-scale value light intensity of the point. The grey-scale value of a single pixel in the reference image can be found in thousands of other pixels in the deformed image. Therefore, a single pixel is not uniquely identifiable. In the so-called “matching process” in DIC, a neighborhood around the pixel of interest, called a subset, with random and unique grey-level intensities, is tracked between the deformed and the reference images (Pan et al. 2009). A region of interest (ROI) needs to be defined first in the reference and deformed images. The ROI is then divided into an evenly spaced grid and the displacement field is calculated at each grid point. The concept of the typical DIC correlation is schematically shown in Fig. 1. A square subset of $(2M + 1) \times (2M + 1)$ pixels is chosen around the point $p(x_i, y_j)$ in the reference image and is used to track its corresponding location in the following deformed images. A correlation criterion is used in the matching process in DIC to evaluate the similarity degree between the reference and the deformed subsets.

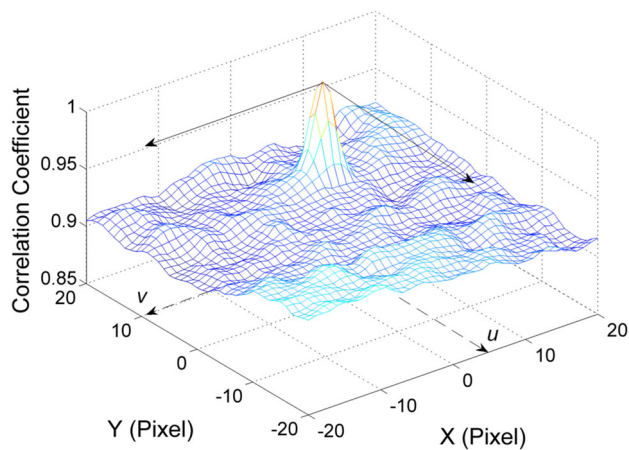


Fig. 2 Correlation coefficient distribution and the matching process

The most commonly used correlation criteria in DIC can be divided into two groups: Cross Correlation criteria (CC) and sum of square differences criteria (SSD) (Giachetti 2000; Tong 2005; Sutton et al. 2007; Pan et al. 2009). Equation (1) describes the correlation coefficient using the CC criterion and Eq. (2) defines the correlation coefficient based on the SSD criterion.

$$C_{CC}(\vec{d}) = \sum_{i=-M}^M \sum_{j=-M}^M [f(x_i, y_j)g(x'_i, y'_j)] \quad (1)$$

$$C_{SSD}(\vec{d}) = \sum_{i=-M}^M \sum_{j=-M}^M [f(x_i, y_j) - g(x'_i, y'_j)]^2 \quad (2)$$

where \vec{d} denotes the displacement vector, M is the subset half size, $f(x_i, y_j)$ is the pixel intensity at coordinate (x_i, y_j) of the reference subset in the reference image and $g(x'_i, y'_j)$ is the pixel intensity at the coordinate (x'_i, y'_j) of the deformed subset in the deformed image (Pan et al. 2009).

There are three different forms of the correlation criterion: the original form [i.e. CC and SSD as shown in Eq. (1) and (2)]; the normalized form (NCC and NSSD); and the zero-normalized form (ZNCC and ZNSSD). The zero-normalized form provides the most accurate noise-proof performance because it is insensitive to the offset and linear scale in the illumination lighting. It is worth noting that the main difference between ZNCC and ZNSSD criteria is the computational cost, which is higher for the ZNSSD criteria than for the ZNCC criteria. The ZNCC criterion is typically 20 % more computationally efficient than the ZNSSD criterion and is commonly preferred for image correlation (Giachetti 2000). The ZNCC criterion was used in this study.

The matching process is performed by searching for the extremum (minimum or maximum) position of the distribution of the correlation coefficient. The coordinates of the extremum position define the new position of the deformed

subset with respect to the reference subset's center. Figure 2 shows a distribution of the correlation coefficient based on the CC criterion and demonstrates how the displacement vector, \vec{d} , is obtained. The same procedure is repeated for the other grid points in the ROI to obtain the full-field displacement.

Two-dimensional DIC is suitable for in-plane deformation and strain measurements of a planar specimen surface. Two-dimensional DIC only needs one fixed camera that is placed perpendicular to the object surface and provides in-plane surface deformations. If the object surface is curved or contains a more complex displacement field, three-dimensional DIC is better suited. It employs two cameras and provides the three-dimensional displacement field of the specimen surface, based on the principle of binocular stereovision (Sutton et al. 2009).

The two-dimensional DIC technique is restricted to planar surfaces with predominant in-plane deformations. However, in actual experiments, out-of-plane deformations are unavoidable and can occur due to several reasons such as seating deformations, Poisson's effect, deviations from planarity, and specimen bending. In the two-dimensional DIC measuring system, the out-of-plane motion of the specimen results in changes in the magnification of the recorded images and induces errors in the calculated in-plane displacement field. Sutton et al. (2008) theoretically demonstrated that the in-plane strain errors due to out-of-plane translations are proportional to $\Delta z/z$, where Δz is the out-of-plane displacement and z is the distance from the object to the camera. This theoretical equation was experimentally verified with rigid body out-of-plane translation experiments (Sutton et al. 2008; Hedayat 2013). Thus, to minimize the effect of out-of-plane motion on two-dimensional DIC measurements, it is suggested that either a standard lens is used and the distance between the object and the lens is increased, or a telecentric lens is used that provides a significantly higher effective lens-object distance (Sutton et al. 2008).

3 Experiments

A series of biaxial compression experiments on gypsum specimens were conducted to investigate the shearing mechanism using active seismic monitoring and DIC technique.

3.1 Specimen Preparation

The material used for the investigation is gypsum which has been extensively used as a rock-model material in other studies (Einstein and Hirschfeld 1970; Reyes and Einstein

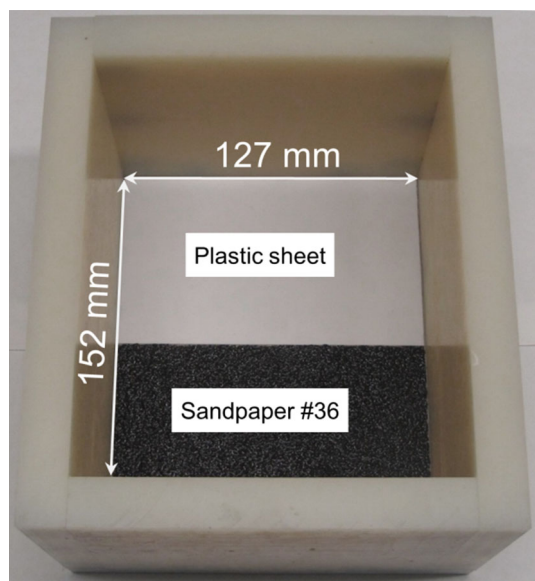


Fig. 3 Mold used for non-homogeneous specimen preparation

1991; Shen et al. 1995; Bobet and Einstein 1998; Mutlu and Bobet 2006). Gypsum is used as the testing material because it has rock-like properties, results in reproducible samples, and can be prepared in a timely and economical manner, and the experiment results can be easily compared with previous findings.

Gypsum specimens were manufactured in the laboratory and consisted of two independent prismatic blocks with dimensions 152.4 mm (6 inch) length, 127 mm (5 inch) wide and 50.8 mm (2 inch) thick. The gypsum material was composed of a mixture of gypsum (Hydrocal B11 from U.S. Gypsum Company), water, and diatomaceous earth, with the following mass proportions: water/gypsum = 0.4; water/diatomaceous earth = 35.

The contact surfaces were made by casting gypsum against flat surfaces with different frictional characteristics. Non-homogeneous contact surfaces were the main focus of this study and consisted of a smooth surface with low frictional strength on the upper half and a rough surface with high frictional strength on the lower half. To produce the non-homogeneous contact surfaces, a smooth plastic sheet was placed on the upper half of a mold and sandpaper, with grit #36 (530 μm), was placed on the lower half of the mold (see Fig. 3). The mold was placed on a vibrating table after filling with gypsum and then vibrated for 5 min to remove any entrapped air. Once the first gypsum block had hardened, a release agent (Product of Dow Corning) was applied to the surface and then the second block was cast against the contact surface of the first block.

This created a two-piece assembly with a perfectly mated interface. The mold release agent prevented

Table 1 Gypsum properties

Properties	Values
Density	1,560 kg/m ³
Unconfined compressive strength	29.81 MPa
Young's modulus	6,780 MPa
Poisson's ratio	0.25
Average compressional wave velocity	3,230 m/s
Average shear wave velocity	1,910 m/s

adhesion between the two blocks and vibration of each single block and the two-block specimen assembly prevented any entrapped air inside the specimen. After the specimen was taken out of the mold, it was stored at room temperature for 24 h, and then placed in an oven for curing at a temperature of 40 °C for 4 days.

After curing the specimen, the sides of the gypsum specimen were carefully polished to obtain flat, smooth and perfectly planar surfaces. The planar surfaces enabled uniform compression loading along the contact surface and application of shear stress parallel to the interface, avoided any stress concentration, and ensured a planar object surface for accurate image correlation.

Image correlation required that the specimen surface had a random speckle pattern and intensity distributions. The final stage of the specimen preparation was to generate the random speckle pattern by spray-painting the surface. The paint deforms together with the surface.

Table 1 summarizes the mechanical and geophysical properties of gypsum. Surface roughness measurements were made over the entire area of each contact surface in 0.25-mm increments in two orthogonal directions using a surface roughness profilometer. Figure 4 shows, individually, the surface roughness for the smooth portion and the rough portion of a discontinuity in a non-homogeneous specimen. The maximum variation in the height of asperities for the smooth and rough surface areas was ± 0.1 and ± 0.4 mm, respectively. As observed in Fig. 4, the fabrication process created homogeneous surfaces, where the roughness was approximately uniformly distributed across the surface. The asperity distribution is presented in Fig. 5, which is a histogram of the frequency distribution of asperity heights, and can be approximated by a normal distribution for both the smooth and rough surfaces. What is interesting is the size of the distribution, which can be evaluated through the standard deviation. The smooth surface has a very narrow distribution with a standard deviation of 0.026 mm, while the rough surface has a much wider distribution, with a much higher standard deviation, 0.129 mm.

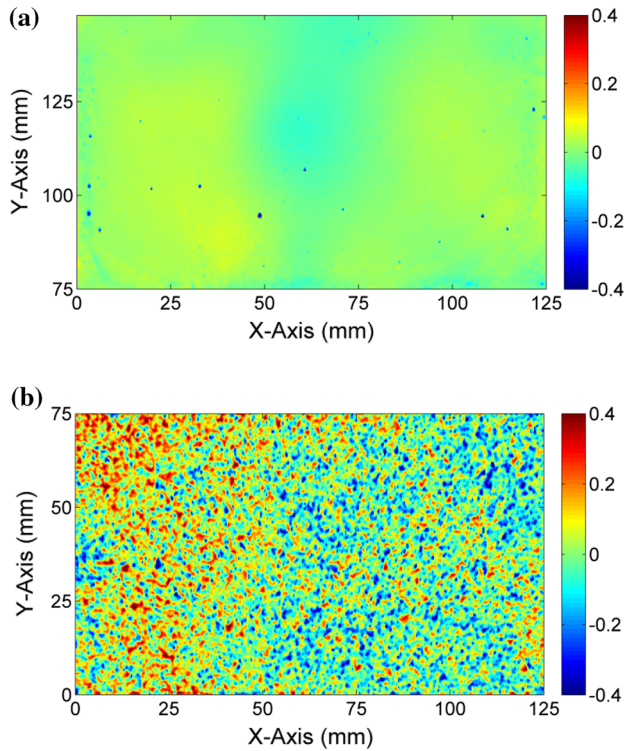


Fig. 4 Contour plot of surface roughness of the interface for a non-homogeneous specimen consisting of **a** smooth (*upper half*) surface (contour values in mm) and **b** rough (*lower half*) surface (contour values in mm)

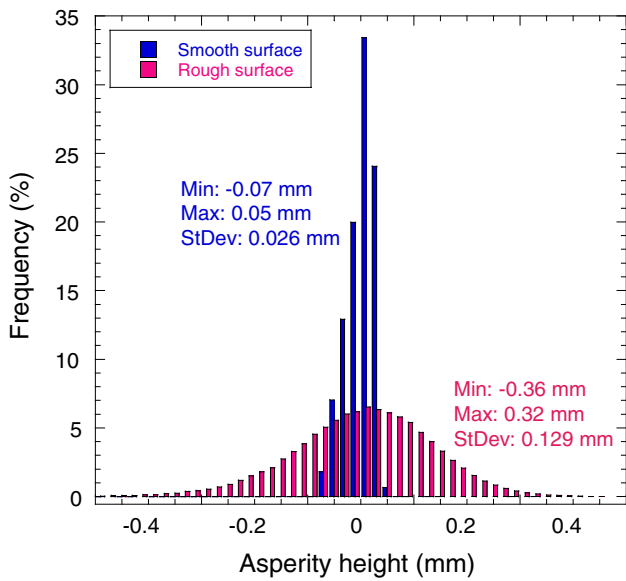


Fig. 5 Histogram of asperity heights for a smooth and a rough surface

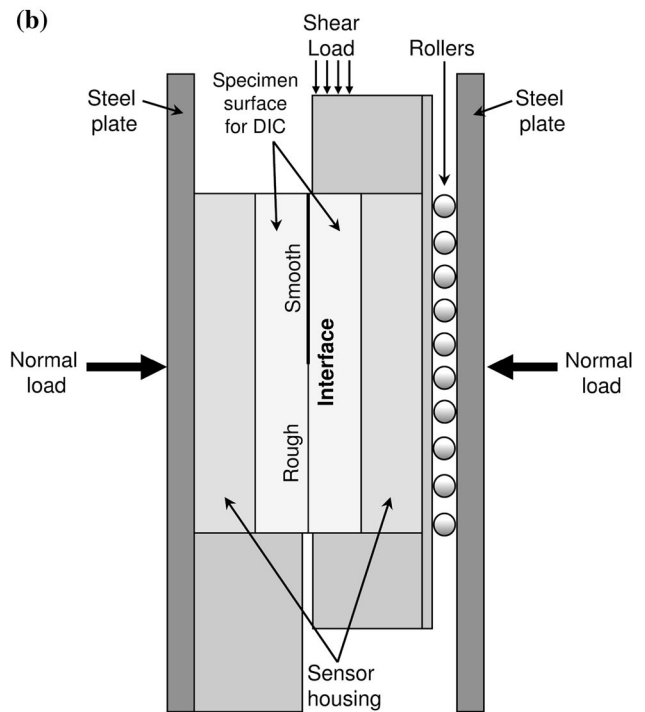
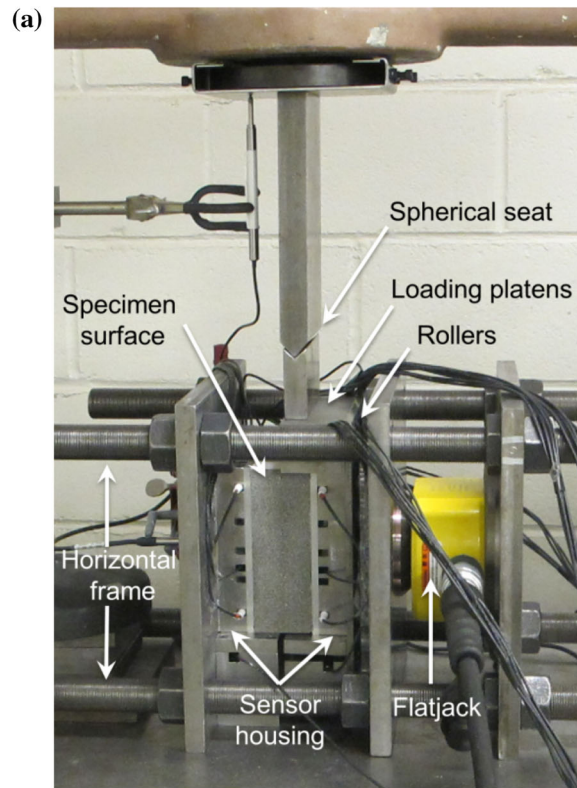


Fig. 6 Experimental setup. **a** Biaxial compression apparatus. **b** Schematic of the loading process

3.2 Experimental Setup

Shear experiments were performed using a biaxial compression apparatus that consisted of two independent loading devices. A horizontal loading frame was used to apply a normal stress to the specimen and a loading machine to apply a shear stress. Figure 6a contains a photograph of the experiment setup. The horizontal frame was composed of a flatjack, loading platens that encase specimen and sensors, steel rods, steel balls, and plates. The flat jack was placed behind the steel plate and, as it was pressurized, transmitted the pressure to the loading plates and the specimen while the horizontal frame supported the reaction. A series of steel balls or rollers were placed between the loading platen and the steel plate to minimize the vertical friction and to ensure that the vertical load was resisted solely by the interface between the blocks. A spherical hinge was created by a wedge connection between the vertical load and the top of the specimen to ensure that the load was aligned with the specimen without any undesired bending moments. Figure 6b is a schematic of the loading apparatus. The experimental setup ensures that the loads that were applied by the horizontal frame and the loading machine were directly transferred to the interface between the gypsum blocks. Compressional and shear wave pulses were transmitted through the discontinuity while the normal and shear loads were applied to the interface.

Special load platens were designed and fabricated to house thirteen transducer pairs, as shown in Fig. 6a. Thirteen sources and 13 receivers were placed on the right and the left side of the gypsum specimen, respectively. The transducers were broadband with a central frequency of 1 MHz (Panametrics V103RM for P-waves and V153RM for S-waves). Figure 7 shows the transducer layout that was used for seismic measurements. In this setup, each platen contained six S-wave transducers and seven P-wave transducers. Four of the S-wave transducers (1S, 6S, 8S, and 9S) were polarized in the direction of shear and two (3S and 7S) were polarized perpendicular to the direction of shear (Fig. 7). Seven P-wave transducers (2P, 4P, 5P, 10P, 11P, 12P, and 13P) were included to monitor changes in normal stiffness. The solid black boxes next to the shear wave transducers in Fig. 7 represent the polarization of the shear waves generated by the transducers. The transducer layouts for source and receiver platens are mirror images of each other.

A pulser–receiver (Panametrics 5077PR) was used to generate square wave pulses with 100 V magnitude with a repetition rate of 5 kHz and a gain of +10 dB. The specimen assembly process was standardized to ensure repeatability of seismic measurements. The transducers were coupled to the surface of the specimens using oven-

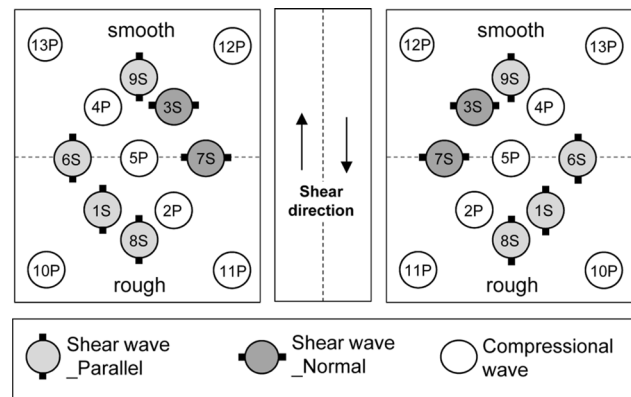


Fig. 7 Experimental setup for seismic transducers

baked honey (Busy Bee Honey) as the coupling medium. The honey was dehydrated at 90 °C for 90 min to reduce its water content. A thin adhesive plastic film was placed on the surface of the specimen to prevent penetration of the honey into the pores of the specimen. A series of repeatability tests was performed with and without the thin plastic film and it was observed that the plastic film had no significant impact on any of the waveform properties. The next step in the experimental setup was to apply a 1 MPa normal stress to the specimen and platens that house the transducers. The load was maintained for 4 h before testing and the transducer signals were monitored to ensure that the coupling between transducers and specimen reached a stable condition. Considering the wave velocity of gypsum, the wavelengths produced by the transducers were 3.2 mm for P-waves and 1.9 mm for S-waves, respectively.

A fast LabView-controlled data acquisition system with sampling rate of 20 Million samples/sec (or 0.05 microseconds per point) recorded full waveforms in real time. For each transducer, 30 transmitted signals were averaged to increase the signal-to-noise ratio. The total time required for the waveform acquisition through all 13 transducers was 0.5 s (i.e. sampling rate of 2 Hz).

A Grasshopper (Point Grey) CCD camera with 2,448 × 2,048 effective square pixels recorded images during the experiment at a rate of 4 frames/sec. The camera remained in a fixed position with respect to the specimen with the optical axis perpendicular to the specimen surface. A 75-mm focal length lens (Model HF75SA1 Fujinon) was used to image the entire 150 mm height of the specimen in focus. The spatial resolution of the imaging system was 80 μm/pixel. The FlyCapture® SDK software was used for controlling the camera and image acquisition. The matching process was performed on the acquired images and the unit of measurement was pixel-based. To transfer the measured values from pixel to the physical dimension, the DIC correlated displacements were multiplied by the

spatial resolution value, $80 \mu\text{m}/\text{pixel}$, to obtain the displacements in the physical dimension.

As noted previously, out-of-plane deformations are inevitable during the shear experiment. The camera was mounted relatively far from the specimen (1.7 m) to minimize the effect of out-of-plane motions on the DIC measurements. A three-dimensional DIC system was used to evaluate the accuracy of the two-dimensional DIC technique and to determine the amount of out-of-plane deformations during a shear experiment. The three-dimensional DIC system used two cameras that enabled measurement of all three components of the displacement vector on the specimen surface. The maximum amount of out-of-plane deformations during the shear experiment was $\Delta z = 0.1$ mm. Considering the distance between the camera and the specimen surface, $z = 1.7$ m, the amount of induced strain error in DIC measurements was equal to $\Delta z/z \approx 5 \times 10^{-5}$, which was in orders of magnitude smaller than the specimen strains. In addition, the displacements measured by the two- and three-dimensional methods were compared and an excellent agreement was found between the two methods denoting that the design of the equipment for two-dimensional displacement measurements was adequate and provided accurate measurements (Hedayat 2013).

4 Experimental Results

In the experiments, specimens were loaded in the biaxial compression apparatus. The normal stress across the surface was applied first and was held constant throughout the duration of a test. Once the desired normal stress was reached, the shear displacement was imposed at a constant displacement rate of $8 \mu\text{m}/\text{sec}$ until failure occurred. Two linear variable differential transducers (LVDTs) placed on top of the specimen recorded the vertical displacement of the specimen while the load cell in the loading machine recorded the applied shear load. Compressional and shear wave pulses were transmitted through the discontinuity while the shear load on the sample was increased and DIC was employed to monitor the discontinuity by measuring the in-plane surface displacements.

Figure 8 contains graphs of shear stress versus shear displacement for a homogeneous smooth, homogeneous rough, and a non-homogeneous gypsum specimen, at a normal stress of 2.3 MPa. The normal stress was kept constant during the experiment and was monitored by a pressure transducer. The shear displacements were measured with respect to the displacement required to reach the peak shear strength to differentiate phenomena prior to and after the peak shear strength. Positive values of shear displacement denote post-peak displacements and negative values denote pre-peak displacements.

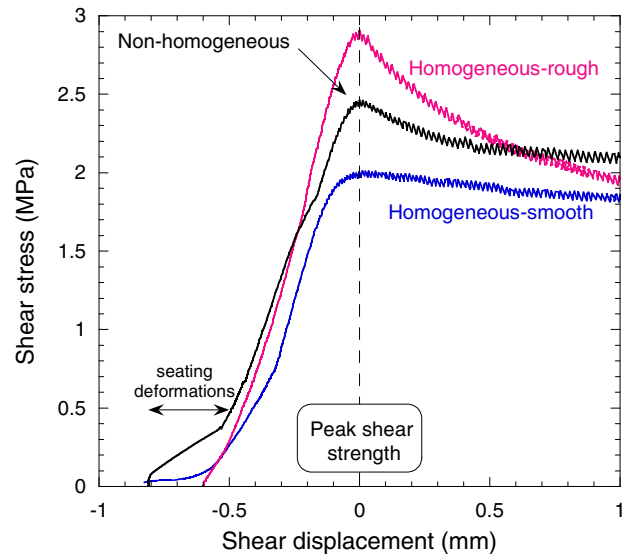


Fig. 8 Shear stress displacement for a non-homogeneous specimen with $\sigma_n = 2.3$ MPa

The data at small shear stresses, i.e. 0–0.5 MPa, are indicative of initial seating deformations caused by the loading machine. After the initial seating deformation, the shear stress showed a steep increase with shear displacement until it reached the peak shear strength. Specimens with homogeneous rough and homogeneous smooth contact surfaces exhibited the largest and the smallest shear strength, respectively. The peak shear strength data correspond to peak friction angles of 38° and 50° for the homogeneous smooth and rough specimens, respectively. The greater the surface roughness of the contact surfaces, the greater the shear strength of the interface.

The transmitted compressional and shear waves recorded from transducers placed on the smooth surface of a non-homogeneous interface during a shear experiment are shown in Fig. 9a, b. The waveforms in Fig. 9 were measured with transducer pairs 4P and 9S at a given shear displacement. As demonstrated in Fig. 8, negative values of shear displacement denote pre-peak displacements and positive values denote post-peak. No significant changes were observed in either the arrival time or frequency content of the recorded signals during the experiment. However, significant changes of peak-to-peak amplitude were observed during shearing. As a result, the peak-to-peak amplitude of the transmitted waves, i.e. the difference between the maximum and the minimum amplitudes of the waveform, was used to study the interface behavior.

Figure 10 contains a graph of shear stress and normalized peak-to-peak amplitudes of shear waves with respect to shear displacement for a non-homogeneous contact surface at a normal stress of 3 MPa. The figure shows peak-to-peak amplitudes from four shear transducers,

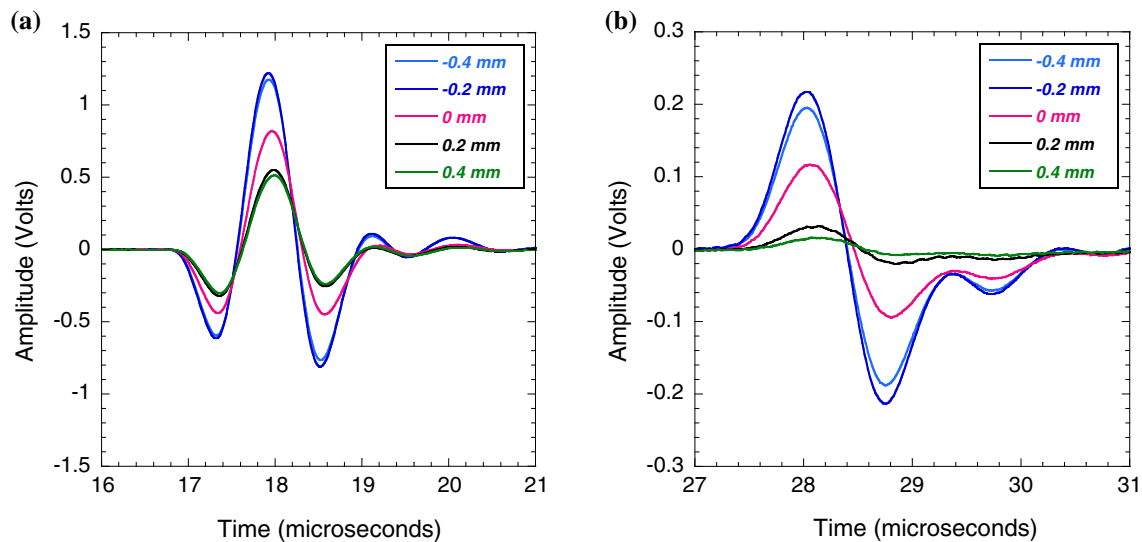


Fig. 9 Transmitted compressional and shear waveforms measured during a shear experiment on a non-homogeneous specimen with $\sigma_n = 2.3$ MPa. **a** Transmitted compressional wave (4P). **b** Transmitted shear wave (9S)

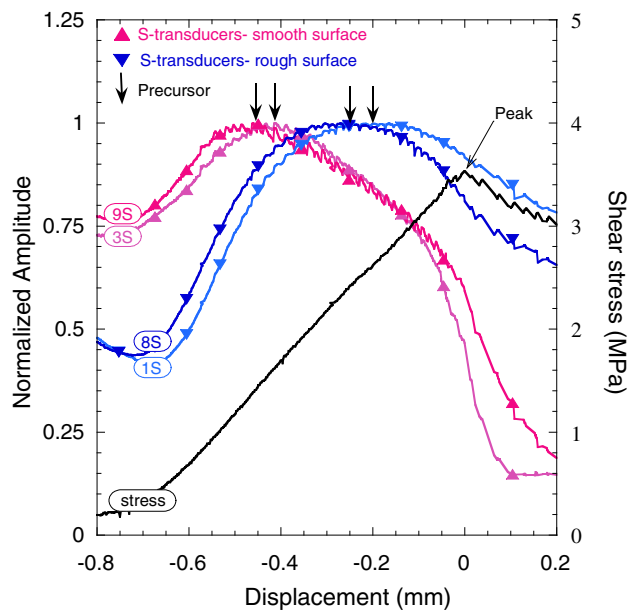


Fig. 10 Shear stress displacement and normalized shear wave amplitudes for a non-homogeneous specimen with $\sigma_n = 3$ MPa

including 3S and 9S on the smooth surface and 1S and 8S on the rough surface, normalized with respect to their maximum values during shearing. Markers with an open triangle pointing upwards are used for transducers placed on the upper half of the specimen (smooth surface) while triangular markers pointing downward represent transducers placed on the lower half (rough surface) of the specimen.

The normalized shear wave amplitude exhibited an increase as the shear load was transferred to the specimen.

A distinct peak in the normalized amplitude recorded on the upper half of the interface, i.e. the smooth area, occurred prior to the peak shear stress followed by a significant drop as slip occurred. Similarly, a distinct peak in the amplitude of the transmitted shear wave recorded on the rough surface occurred prior to the peak shear stress. Peaks in the normalized shear wave amplitude are very specific attributes that are consistently observed prior to the peak shear strength for homogeneous and non-homogeneous contact surfaces and so are taken as “precursors” to failure of the frictional interface (Hedayat 2013). The change of amplitude is related to the fracture stiffness and the fracture stiffness, as expected, increases with shear, but at some point, reaches a maximum. Shearing of micron and submicron asperities prior to failure is a likely source of the increase in shear stiffness that gives rise to the observed precursors.

A similar behavior, although more attenuated, was observed in the P-wave data. The amplitude of the P-waves, in contrast to those of the S-waves, did not increase as the shear load was applied. P-waves provide a measure of fracture’s normal stress while S-waves provide a measure of fracture’s shear stress. The application of shear load has a significant effect on the fracture’s shear stiffness and therefore is more clearly observed by S-wave transducers than P-wave transducers.

In experiments performed on specimens with homogeneous contact surfaces, precursors were observed to occur between -0.2 and 0 mm before the peak shear strength of the smooth surface and between -0.3 and -0.1 mm before the peak shear strength of the rough surface. Due to the close distance between precursors and failure of the smooth

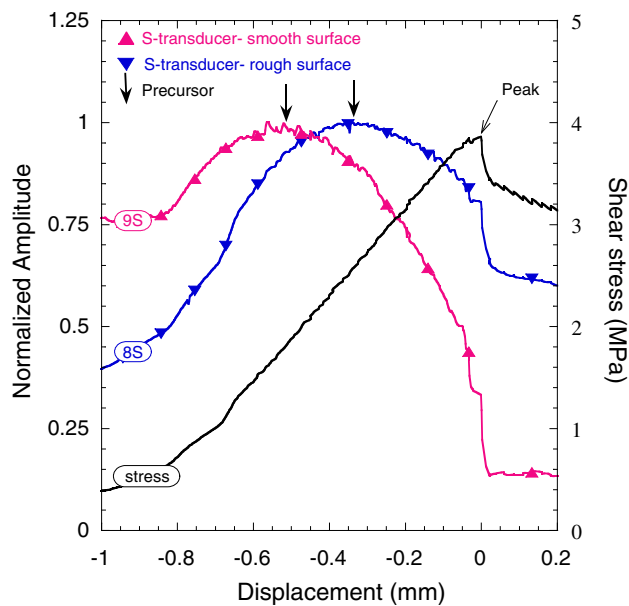


Fig. 11 Shear stress displacement for a non-homogeneous specimen with $\sigma_n = 3$ MPa

surface, and the larger distance between precursors and failure of the rough surface, precursors can be used to investigate the sequence of local slip events that occurred along the interface even for a complex slip pattern. As seen in Fig. 10, the precursors for the smooth surface were observed around -0.45 mm of shear displacement while the precursors for the rough surface around -0.22 mm. Due to the smaller distance (i.e. -0.2 to 0 mm) between the precursors and the peak shear strength of the smooth surface, it is concluded that slip occurred first along the smooth surface. The larger distance (i.e. -0.3 to -0.1 mm) between the precursors and the peak shear strength of the rough surface indicate that slip occurred later along the rough surface.

DIC measurements can also be used to track slip along the contact surface and to confirm the previous conclusion of sequential slip observed in the seismic measurements. A series of experiments was performed utilizing the active seismic monitoring and the DIC technique. Figure 11 shows the results of an additional experiment performed on a non-homogeneous contact surface at a normal stress of 3 MPa. Similar to the observations made on Fig. 10, seismic precursors were observed prior to the failure of the interface.

Figure 12 shows the sequence of vertical displacement contours for two non-homogeneous specimens. Figure 12a shows the sequence of vertical displacement contours for an experiment in which the smooth surface was placed at the top and the rough surface placed at the bottom. Figure 12b shows the results of an experiment with the rough surface at the top and the smooth surface at the bottom.

Slip is defined as the relative displacement across the discontinuity or the interface. The displacement contours consist of a series of color bands, each representing the vertical displacement field at a given shear stress. Positive values of vertical displacement indicate downward movement.

Figure 12(a-1) shows the vertical displacement contours when the precursors on the smooth surface occurred (at 45 % of the shear strength). A discontinuity in the vertical displacement contour plot can be observed at the top of the specimen [top of Fig. 12(a-1)], i.e. slip initiates in the smooth area close to the application of the shear load. As the shear load is increased to 65 % of the shear load, slip further advances along the smooth area, as shown in Fig. 12(a-2). This is the moment when precursors for the rough surface were observed. At the peak shear load, slip fully developed along the smooth area and propagated to the rough area, as shown in Fig. 12(a-3).

Figure 12b shows the sequence of displacement contours for the experiment with the rough surface at the top and the smooth surface at the bottom. Slip initiated from the smooth area at the bottom of the specimen and also from the rough area, close to the application of the shear load. Interestingly enough, as the shear load was increased, slip further advanced along the smooth area, as shown in Fig. 12(b-2). At the peak shear load, slip fully developed along the smooth area and propagated to the rough surface, as shown in Fig. 12(b-3).

To quantify the amount of slip as a function of position along the interface, profiles of vertical displacement were extracted from the displacement contours (Fig. 12a). As mentioned earlier, the displacement measurement with DIC involves matching subsets of images through a matching process. This cannot be easily done at the interface because of the large displacement gradient. Instead, two vertical sections at a short distance (32 pixels or 2.56 mm away from the interface) were selected to determine the slip along the interface (these sections are indicated by the vertical dashed lines in Fig. 12a).

Figure 13 shows slip along the interface as a function of the imposed shear displacement. As already mentioned, shear displacements were measured with respect to the displacement required to reach the peak shear strength. Slip was larger in the smooth area than in the rough area as failure approached. Because the line series are indicative of slip at equal shear displacement increments, they also provide a measure of the rate of slip across the interface. The rate of slip was considerably faster in the smooth region than in the rough region.

To couple the geophysical observations with DIC measurements, the normalized amplitude of shear wave transducers is compared with the corresponding slip from DIC in Fig. 14. The seismic transducers are essentially

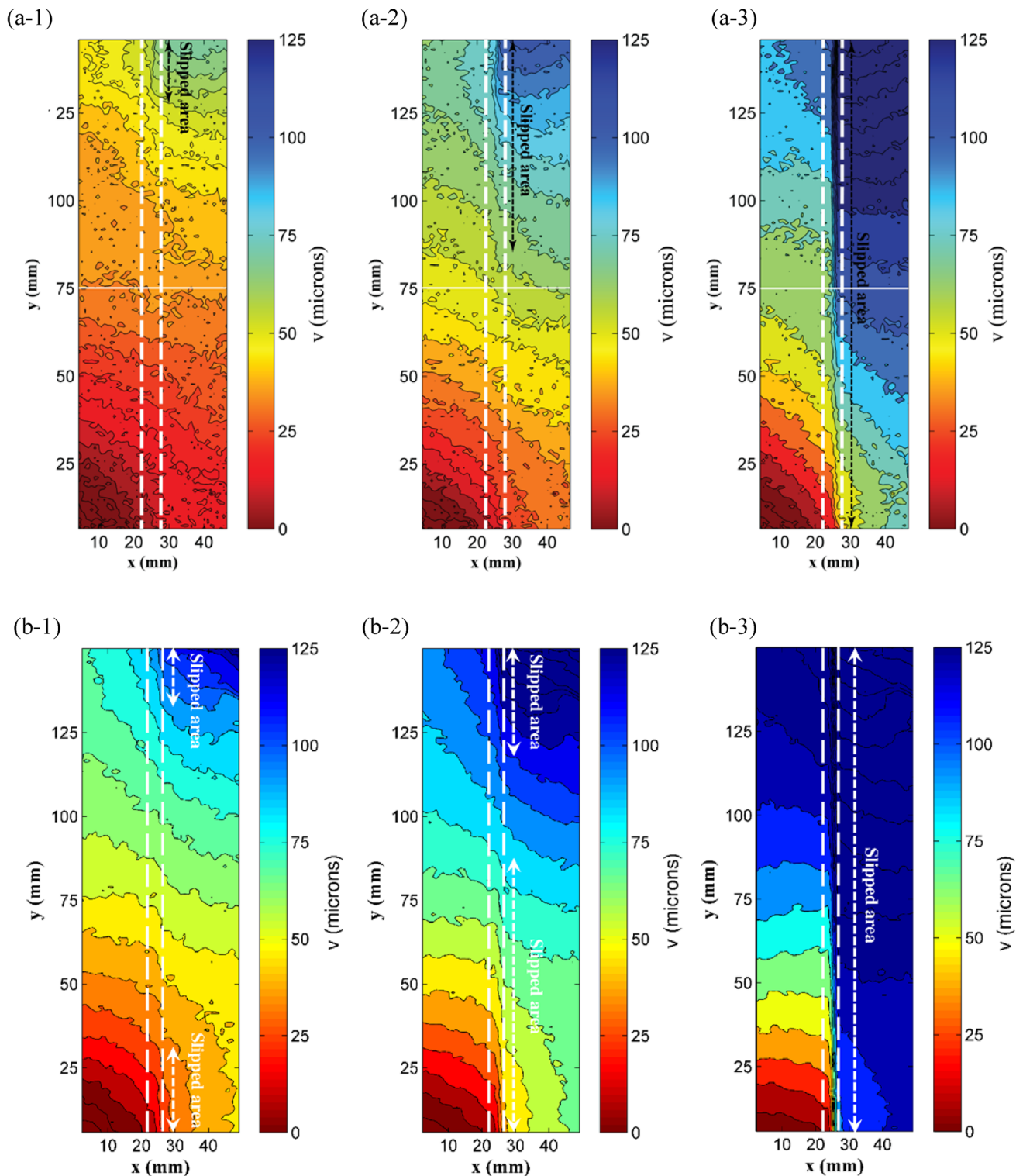


Fig. 12 Vertical displacement contours during the shear experiments with **a** smooth surface on the top and rough surface on the bottom. **a-1** -0.5 mm (45% of peak load), **a-2** -0.33 mm (65% of the peak

load), **a-3** 0 mm (Peak load); **b** rough surface on the top and smooth surface on the bottom. **b-1** 45% of peak load, **b-2** 65% of the peak load, **b-3** Peak load

ultrasonic sensors that probe changes in the interface. Each transducer only probes the area that is within its beam diameter and lobe pattern. Thus, a comparison of the

transducer readings with vertical displacements is made for locations on the specimen surface that corresponds to the location (in terms of height) of the transducer pair. Slip, as

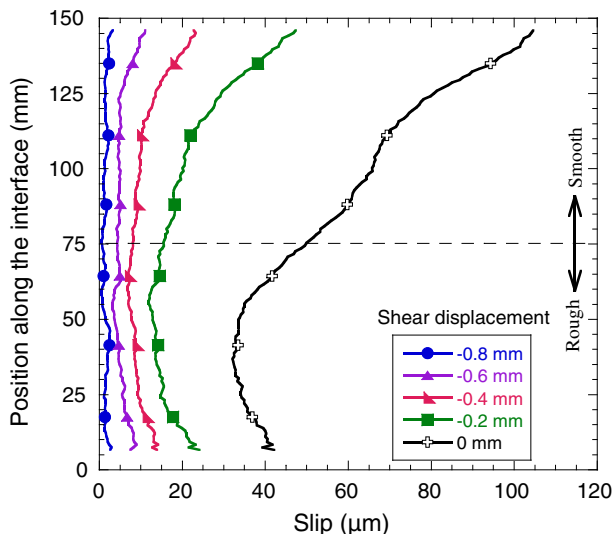


Fig. 13 Slip profile along an interface with non-homogeneous contact surface

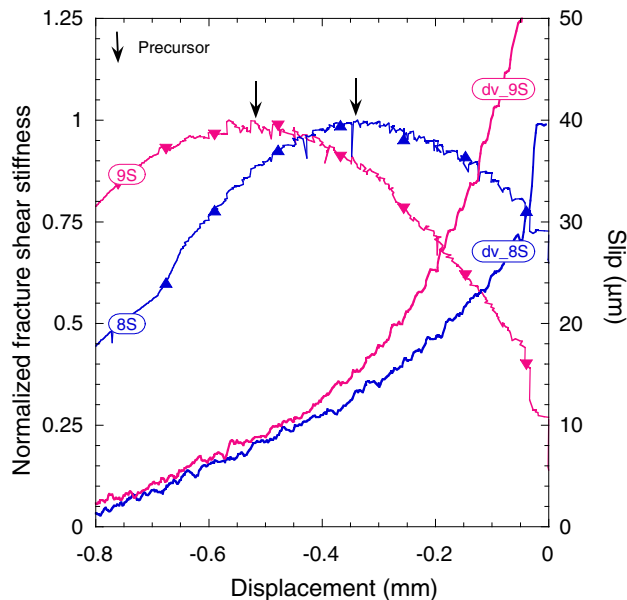


Fig. 15 Fracture shear stiffness and slip along the discontinuity

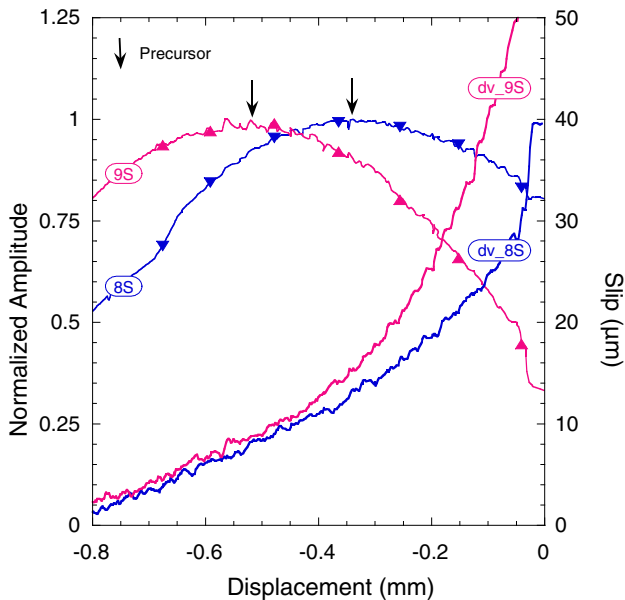


Fig. 14 Precursors and slip along the discontinuity

a function of applied shear stress, is extracted from Fig. 13 at the location that is illuminated by the transducer. In Fig. 14, normalized peak-to-peak amplitudes of the waveforms measured by transducer pair 9S on the smooth surface and 8S on the rough surface are shown along with their corresponding vertical displacements. In the figure, the green arrows denote the change in rate of displacement and are associated with the instant when slip starts at a particular point, as observed in the DIC measurements. Slip initiated first in the smooth surface and was concurrent with the precursor from the seismic transducer. The

increase in the rate of slip occurred later for the rough surface and was also associated with the corresponding seismic precursor.

It is hypothesized that the changes observed in peak-to-peak amplitude during shear were the result of local mechanical changes of the frictional surface. The seismic response of a fracture can be theoretically evaluated using the displacement discontinuity model (Schoenberg 1980; Pyrak-Nolte et al. 1990; Pyrak-Nolte 1996; Cook 1992; Hildyard et al. 2005). In the model, a fracture is represented as a displacement discontinuity at the boundary between two elastic half spaces, with negligible thickness compared to the wavelength of the seismic waves. The boundary conditions that describe the displacement discontinuity are (a) the stress across the boundary is continuous and (b) the displacements are discontinuous. The magnitude of the displacement discontinuity is inversely proportional to the specific stiffness of the fracture. Thus, changes in the amplitude of transmitted waves are associated with changes in the specific stiffness of the discontinuity. The fracture shear specific stiffness was computed from the transmission coefficient T , using the relationship (Pyrak-Nolte 1996):

$$\kappa_s = \frac{\omega \rho V_s}{2} \frac{|T|}{\sqrt{1 - |T|^2}} \tag{3}$$

where ρ and V_s are the density and shear wave velocity of the gypsum, respectively, and ω is the angular frequency.

Equation (3) was used to calculate fracture shear specific stiffnesses that are shown in Fig. 15. In the figure, the shear specific stiffness for each transducer location is normalized with respect to the transducer’s maximum value during

shearing. The calculated maximum shear specific stiffness for transducer 9S that sampled the smooth surface was 0.34 TPa/m, while the maximum shear stiffness of the rough surface was 2.98 TPa/m based on transducer 8 measurements. Interestingly, the fracture specific stiffness increases with shear until it reaches a maximum (the precursor), after which it decreases for both smooth and rough contact surfaces. Thus, it is concluded that the precursors are associated with changes in frictional characteristics of the contact surfaces and are indicative of a significant reduction in fracture shear stiffness. This is further supported by DIC measurements. Indeed, the static shear stiffness of a fracture is defined as the ratio of an increment in the contact shear stress to the corresponding increment in shear displacement. The increase in the rate of slip indicates a reduction in fracture shear stiffness.

5 Conclusions

This study used seismic wave transmission and digital image correlation to understand the slip mechanisms along frictional discontinuities. A number of biaxial compression experiments were performed on gypsum specimens with non-homogeneous contact surfaces. Distinct peaks in the amplitude of the transmitted waves were observed prior to the peak shear strength and were defined as “precursors” to the failure. The precursors indicated that slip initiated at the smooth surface and then extended to the rough surface, as the shear load was increased. DIC measurements were also used to track slip along the contact surface. Slip was identified as a jump in the displacement field across the discontinuity. The DIC measurements also confirmed that slip initiated at the smooth surface and propagated to the rough surface. Precursors were associated with an increase of the rate of slip across the discontinuity and, as confirmed by the DIC measurements, were linked to a reduction of the fracture’s shear stiffness. Precursors have significant potential for providing data on engineering properties of fractures such as specific stiffness and for predictive capabilities for early warning of failures (e.g., earthquakes) and other instabilities due to shear failure of a frictional discontinuity.

Acknowledgments This research has been supported by the National Science Foundation, Geomechanics and Geotechnical Systems Program, under grant CMS-0856296.

References

- Barton N (1976) Review of a new shear strength criterion for rock joints. *Eng Geol* 7:287–332
- Barton N, Choubey V (1977) The shear strength of rock joints in theory and practice. *Rock Mech* 10:1–54
- Bobet A, Einstein HH (1998) Fracture coalescence in rock-type materials under uniaxial and biaxial compression. *Int J Rock Mech Min* 35(7):863–888
- Brady BHG, Brown ET (2004) *Rock mechanics for underground mining*. Kluwer Academic Publishers, The Netherlands
- Bürgmann R, Pollard D, Martel SJ (1994) Slip distributions on faults: effects of stress gradients, inelastic deformation, heterogeneous host-rock stiffness, and fault interaction. *J Struct Geol* 16:1675–1690
- Byerlee J (1978) A review of rock mechanics studies in the United States pertinent to earthquake prediction. *Pure Appl Geophys* 116:586–602
- Chen WY, Lovell CW, Haley GM, Pyrak-Nolte LJ (1993) Variation of shear-wave amplitude during frictional sliding. *Int J Rock Mech Min* 30:779–784
- Chu TC, Ranson WF, Sutton MA, Peters WH (1985) Applications of digital-image-correlation techniques to experimental mechanics. *Exp Mech* 25:232–244
- Comninou M, Dundurs J (1983) Spreading of slip from a region of low friction. *Acta Mech* 47:65–71
- Cook NGW (1992) Natural joints in rock: mechanical, hydraulic and seismic behavior and properties under normal stress. *Int J Rock Mech Min* 29(3):198–223
- De Bremaecker JCI (1987) Thrust sheet motion and earthquake mechanisms. *Earth Planet Sci Lett* 83:159–166
- Dieterich JH (1979) Modeling of rock friction I: experimental results and constitutive equations. *J Geophys Res* 84:2161–2168
- Einstein HH, Hirschfeld RC (1970) Model studies on mechanics of jointed rocks. *ASCE J Geotech Div* 99:229–248
- Giachetti A (2000) Matching techniques to compute image motion. *Image Vision Comput* 18:247–260
- Gorbatikh LB, Nuller D, Kachanov M (2001) Sliding on cracks with non-uniform frictional characteristics. *Int J Solids Struct* 38:7501–7524
- Hedayat A (2013) *Mechanical and geophysical characterization of damage in rocks*. Dissertation, Purdue University
- Hildyard MW, Young RP, Collins DS, Pettitt WS (2005) Seismic wave propagation to diagnose the state of fracturing. *J S Afr Inst Min Metall* 105:437–446
- Hudson JA (1981) Wave speeds and attenuation of elastic waves in material containing cracks. *Geophys J Int* 64:133–150
- Jaeger JC (1971) Friction of rocks and stability of rock slopes. *Geotechnique* 21:97–134
- Jaeger JC, Cook NGW, Zimmerman RW (2007) *Fundamentals of rock mechanics*. Wiley-Blackwell, London
- Johnston MJS, Linde AT, Gladwin MT, Borchardt RD (1987) Fault failure with moderate earthquakes. *Tectonophysics* 144:189–206
- King MS, Myer LR, Rezowalli JJ (1986) Experimental studies of elastic-wave propagation in a columnar-jointed rock mass. *Geophys Prospect* 8(34):1185–1199
- Kulatilake PHSW, Shou G, Huang TH, Morgan RM (1995) New peak shear strength criteria for anisotropic rock joints. *Int J Rock Mech Min* 32:673–697
- Ladanyi B, Archambault G (1969) Simulation of the shear behaviour of a jointed rock mass. In: 11th US symposium on rock mechanics, Berkeley, 105–125
- Lin Q, Labuz JF (2013) Fracture of sandstone characterized by digital image correlation. *Int J Rock Mech Min* 60:235–245
- Liu J, Iskander M (2004) Adaptive cross correlation for imaging displacements in soils. *J Comput Civil Eng* 18:46–57
- Lockner D (1993) The role of acoustic emission in the study of rock fracture. *Int J Rock Mech Min* 30:883–899
- Malanchuk NI (2011) Local slip of bodies caused by the inhomogeneous friction coefficient. *Mater Sci* 46:543–552
- Mutlu O, Bobet A (2005) Slip initiation on frictional fractures. *Eng Fract Mech* 72:729–747

- Mutlu O, Bobet A (2006) Slip propagation along frictional discontinuities. *Int J Rock Mech Min* 43:860–876
- Nagata K, Nakatani M, Yoshida S (2008) Monitoring frictional strength with acoustic wave transmission. *Geophys Res Lett* 35:L06310
- Orteu JJ (2009) 3-D computer vision in experimental mechanics. *Opt Laser Eng* 47:282–291
- Pan B, Qian K, Xie H, Asundi A (2009) Two-dimensional digital image correlation for in-plane displacement and strain measurement: a review. *Meas Sci Technol* 20(6):062001
- Price RA (1988) The mechanical paradox of large overthrusts. *Geol Soc Am Bull* 102(4):529–532
- Pyrak-Nolte LJ (1996) The seismic response of fractures and the interrelations among fracture properties. *Int J Rock Mech Min* 33(8):787–802
- Pyrak-Nolte LJ, Myer LR, Cook NGW (1990) Transmission of seismic-waves across single natural fractures. *J Geophys Res* 95:8617–8638
- Rechenmacher AL, Finno RJ (2004) Digital image correlation to evaluate shear banding in dilative sands. *Geotech Test J* 27:13–22
- Reyes O, Einstein HH (1991) Failure mechanism of fractured rock- a fracture coalescence model. In: Proceedings of the 7th ISRM congress Aachen, Germany, September 16–20
- Schoenberg M (1980) Elastic wave behaviour across linear slip interfaces. *J Acoust Soc Am* 68(5):1516–1521
- Shen B, Stephansson O, Einstein HH, Ghahreman B (1995) Coalescence of fractures under shear stress experiments. *J Geophys Res* 100:5975–5990
- Sibson RH (1989) Earthquake faulting as a structural process. *J Struct Geol* 11:1–14
- Sutton MA, Yan J, Deng X, Cheng CS, Zavattieri P (2007) Three-dimensional digital image correlation to quantify deformation and crack-opening displacement in ductile aluminum under mixed-mode I/III loading. *J Opt Eng* 46(5):051003
- Sutton MA, Yan JH, Tiwari V, Schreier WH, Orteu JJ (2008) The effect of out-of-plane motion on 2D and 3D digital image correlation measurements. *Opt Laser Eng* 46:746–757
- Sutton MA, Orteu J, Schreier HW (2009) Image correlation for shape, motion and deformation measurements. Springer, New York
- Tong W (2005) An evaluation of digital image correlation criteria for strain mapping applications. *Strain* 41:167–175
- Withers P (2008) Strain measurement by digital image correlation. *Int J Exp Mech* 44:421–422
- Yoshika N, Scholz CH (1989) Elastic properties of contacting surfaces under normal and shear loads: comparison of theory with experiment. *J Geophys Res* 94:17691–17700